RECENT ADVANCES IN MODELING AND SIMULATIONS OF MULTIPHASE FLOWS

Effect of particle shape on bedload sediment transport in case of small particle loading

Ramandeep Jain · Silvio Tschisgale · Jochen Fröhlich

Abstract The paper presents four direct numerical simulations of an open channel flow with geometrically resolved particles heavier than the fluid. In each simulation the same number of mono-disperse particles is considered, with the shape of the particles varied between the simulations, while conserving the volume. Three simulations are reported with non-spherical particles, here prolate ellipsoid, oblate ellipsoid, and Zingg-ellipsoid, and compared to a fourth one with spherical particles. The influence of the particle shape on the average fluid motion and on the disperse particle phase is investigated in the regime of low particle loading. It is found that the Reynolds stresses with spherical particles are much smaller compared to those with non-spherical particles. Of these, they are maximum in the case of oblate particles. Furthermore, the oblate spheroids are prominently found in the near-wall region and hardly roll. This behavior differs markedly from the behavior of the spherical particles, which preferably bounce and roll. The other two cases, with prolate ellipsoids and Zingg-ellipsoid behave between the two extreme cases of spherical and oblate particles. The oblate spheroids orient such that their symmetry axis is parallel to the

wall-normal direction, whereas the prolate spheroids orient with their symmetry axis parallel to the streamwise direction. The Zingg-ellipsoids orient with their longest axis parallel to the streamwise direction and their smallest axis parallel to the wall-normal direction. This preferred orientation is more dominant in the near wall region. All effects mentioned are supported by quantitative evaluation of statistics and can serve as reference for future validations.

Keywords Direct numerical simulation · Sediment transport · Non-spherical particles · Particle laden flows

1 Introduction

Bed load transport of particles in a viscous fluid, mostly under turbulent conditions designates the situation where non-buoyant particles are transported along a smooth or rough bottom wall with fluid forces and gravity in a relation such that the fluid forces are strong enough to move the particles while gravity is strong enough to retain the particles within a comparatively small elevation from the bottom wall. Examples are sediment transport in rivers [7, 35] and oceans [42] in case of current near the bed, transport in pipelines [39] or by hydraulic transport in process

R. Jain · S. Tschisgale · J. Fröhlich (✉)
Institute of Fluid Mechanics, Technische Universität
Dresden, George-Bähr Str. 3c, 01062 Dresden, Germany
e-mail: ramandeep.jain@tu-dresden.de

e-mail: ramandeep.jain@tu-dresden.de

engineering [44], as well as pneumatic transport of particles by an air stream [43], to name but a few.

Bed-load transport of particles can be observed in liquids and gases, as illustrated by the list of examples. With usual particles, like sand etc., the situations is, however, somewhat different in these two cases because of the larger density difference with gas flows which often result in higher Stokes numbers and reduced dependency on viscous forces. While occasionally addressing pneumatic or aeolian transport where appropriate, this paper focuses on hydraulic transport, i.e. the situation where viscous forces are important and need to be accounted for by a computational model.

With bedload transport the trajectory of a moving particle consists of three phases. (1) Entrainment, (2) dislocation, which in turn can be subdivided into rolling, sliding, and jumping, and (3) deposition. The fact that the overall trajectory as well as the individual phases named depend on the particle shape has been observed in a huge number of studies, e.g. [1, 12, 32, 34, 38].

Entrainment Most often in the literature, entrainment is assessed by the critical Shields stress, which quantifies the ratio of the shear stress due to fluid to the particle weight. However, experiments exhibit a wide spread results for a particular particle Reynolds number defined using the median grain size of the sediment bed in the original experiments of [49]. This can be explained by the fact that particles of different shapes but same weight experience different drag forces at the same particle Reynolds number [8, 20, 45]. Hottovy and Sylvester [20] reported a 100% increase in drag coefficient in case of irregular shapes, compared to a spherical particle. Additionally, the drag also depends upon the orientation of a particle [8, 45].

Dislocation Numerous experiments have been conducted to examine the actual particle motion during bedload transport, e.g. [1, 7, 34, 35, 43]. One of the earliest studies was conducted by Krumbein [34] using ellipsoids made of cement mortar, where he observed that the spherical particles have the largest streamwise particle velocity for a given Froude number, while disk shaped particles moved slowest among the shapes investigated. Lane and Carlson [35] reported that the spherical particles are easier to move than disk shaped particles of equal weight. In contrast, Bradley et al. [7] in his study on Knik river, Alaska, US observed that the platy shaped particles were the most transportable among the three lithologies examined. Interestingly, Abbott and Francis [1] reported a

mere 2% variation in the saltation height and length of three different shaped particles.

Deposition Whether a jumping particle gets deposited or not depends to a large extent on the fact whether the collision with the sediment bed is elastic or inelastic. Many authors noticed that the collision between non-spherical particles are prominently inelastic [1, 15]. Under the same hydraulic conditions, only 5 impacts out of 59 were seen to result in a clear rebound observed in the experiments of Abbott and Francis [1]. On the contrary, only few authors reported that the collisions are partially elastic with a small rebound of the colliding particle, like Niño et al. [38]. Schmeeckle et al. [47] proposed that the collisions are mainly inelastic due to off-center collisions, in which the particle center keeps moving towards the wall even if there is a rebound of the contact point after the collision. The present authors explored the phenomenon numerically and found that, indeed, the effective restitution coefficient depends upon the orientation of the colliding particles [24].

All the phenomena mentioned above are influenced by the orientation of a non-spherical particle. Recently conducted numerical studies on particles with smaller density, i.e. non-buoyant particles have revealed a particular orientation of the particles in the near wall region depending upon their shape [4, 5, 17, 18]. It was found that oblate spheroids are aligned with their symmetry axis in the wall-normal direction. In contrast, prolate spheroids orient their axis in the streamwise direction. Additionally, this preferential orientation becomes more prominent as the particles approach the wall. Such a phenomenon, if noticed also in case of heavy particles at higher Stokes number, together with the results presented in [24], can explain why in many experiments a particle did not rebound after a collision.

Not only are the particle transport properties influenced by the particle shape, also the behavior of the surrounding fluid phase changes drastically depending on the particle shape [6, 16, 26, 46, 48]. The wake behind a single fixed spherical, oblate, and prolate particle was examined by Johnson and Patel [26], Shenoy and Kleinstreuer [48], and El Khoury et al. [16] at moderate particle Reynolds number Re_p of up to 300. Shenoy and Kleinstreuer [48] reported double-sided hairpin vortices shed from diametrically opposite locations in the wake of a disk at $Re_p \approx 155$. Also,

the separation zone was periodically rotating making the flow three-dimensional and more turbulent. These observations are in contrast to the one-sided shedding of vortices noticed in the wake of a sphere [26, 46]. Similarly, the wake observed past a prolate with its maximum projection area oriented perpendicularly to the flow is noticeably different from the wake seen behind a sphere [16]. The difference in the wake behind a moving particle in bedload transport due to its shape can create three dimensional fluid structures in the near wall region. Furthermore, the strong non-uniformity in vertical direction and the presence of surrounding particles introduce additional complexity. The momentum transferred by such instantaneous turbulent forces is important in determining the entrainment of a sediment grain [14, 55].

The impact of particle shape on bed-load transport so far has mostly been studied experimentally. To the best of the authors' knowledge, there are only two simulations of bed-load transport with non-spherical particles in the literature [19, 51]. In both simulations, the fluid phase is resolved using large-eddy simulation and a non-spherical particle was represented as a cluster of spherical particles. In the first reference, the trajectories of a spherical and a non-spherical particle were compared. It was found that the trajectory of a non-spherical particle is more dispersive and has more jumps as compared to the trajectory of a spherical particle [19]. In the second reference, it was seen that the spherical particles have the least rotational velocity among the shapes simulated [51]. Recently conducted direct numerical simulations with resolved particles on sediment transport provide high fidelity datasets to understand the physics of particle-laden flow, e.g. [11, 23, 30, 31, 41, 50, 55]. These, however, only relate to monodisperse spherical particles. In the present work, the numerical framework of DNS combined with Immersed Boundary Method (IBM) is applied to systematically explore the effect of particle shape on its motion in case of small particle loading.

2 Numerical method and collision model

2.1 Fluid phase

The continuous phase is governed by the unsteady, three-dimensional Navier-Stokes equations for incompressible fluids

$$\frac{\partial \mathbf{u}}{\partial t} = -\nabla \cdot (\mathbf{u} \otimes \mathbf{u}) + \frac{1}{\rho_\text{f}} \nabla \cdot \boldsymbol{\tau} + \mathbf{f}_\text{v} + \mathbf{f}_\text{IBM} , \qquad (1)$$

$$\nabla \cdot \mathbf{u} = 0. \qquad (2)$$

A coordinate system is defined such that x, y, and z are the streamwise, wall-normal, and spanwise directions, respectively. The notation $\mathbf{u} = (u, v, w)^T$ designates the velocity vector with its components in x-, y-, and z-direction, respectively, p is the pressure, ρ_f the fluid density, and t the time. The particle-fluid interaction is modeled by a new IBM which is based on a judicious determination of the coupling force $\mathbf{f}_\text{IBM}$ located at the phase boundaries, i.e. the particle surfaces [52]. The flow is driven by a spatially constant specific volume force $\mathbf{f}_\text{v}(t)$. The hydrodynamic stress tensor $\boldsymbol{\tau}$ is

$$\boldsymbol{\tau} = -p \, \mathbb{I} + \mu_\text{f} \left(\nabla \mathbf{u} + (\nabla \mathbf{u})^\top \right). \qquad (3)$$

Here, μ_f is the dynamic viscosity of the fluid, and $\mathbb{I}$ the identity matrix. These equations are solved on a staggered Cartesian grid using a second-order Finite Volume Method in space and time as described in [29]. The stepsize in space, Δx, is identical in all three directions. The convective term in Eq. (12) is handled using an explicit three-step third-order low-storage Runge-Kutta scheme and a Crank-Nicolson scheme is executed for the viscous terms in each substep, as well as a pressure correction step in each substep.

2.2 Disperse phase

The equations of motion of a particle are

$$m_\text{p} \frac{\text{d}\mathbf{u}_\text{p}}{\text{d}t} = \int_\Gamma \boldsymbol{\tau} \cdot \mathbf{n} \, \text{d}S + \mathbf{f}_\text{c} + \mathbf{f}_\text{lub} \\ + V_\text{p} (\rho_\text{p} - \rho_\text{f}) (\mathbf{g} + \mathbf{f}_\text{v}) , \qquad (4)$$

$$\frac{\text{d}(\mathbf{i}_\text{p}\boldsymbol{\omega}_\text{p})}{\text{d}t} = \int_\Gamma \mathbf{r} \times (\boldsymbol{\tau} \cdot \mathbf{n}) \, \text{d}S + \mathbf{m}_\text{c} + \mathbf{m}_\text{lub} , \qquad (5)$$

which are solved for each individual particle. Here, m_p, V_p, and ρ_p are the mass, volume, and density of the particle, respectively, $\mathbf{u}_\text{p}$ the particle velocity, Γ the particle surface, $\mathbf{n}$ the outward-pointing unit normal vector on Γ, $\mathbf{g}$ the gravitational acceleration, $\mathbf{f}_\text{v}$ the same specific volume force as in Eq. (12), $\mathbf{f}_\text{c}$ the collisional force, and $\mathbf{f}_\text{lub}$ the lubrication force. In the angular momentum balance $\mathbf{i}_\text{p}$ is the tensor of inertia of the particle, $\boldsymbol{\omega}_\text{p}$ the angular velocity, $\mathbf{r}$ the position

vector connecting the particle center of mass with a point on the particle surface. Finally, $\mathbf{m}_c$ and $\mathbf{m}_{lub}$ are the torques caused by the collision and the lubrication forces, respectively.

The fluid-particle coupling is achieved by a newly developed Immersed Boundary Method (IBM) [52]. This allows the numerically efficient simulation of a large number of mobile particles with spatially resolved geometry.

To numerically represent the fluid-particle interaction N_L Lagrange marker points were distributed over the surface of the particles. For this purpose, an open source code provided by Persson and Strang [40] was used.

2.3 Collision model

For particle-particle interaction via collisions, a constraint-based collision model was employed accounting for all forces acting during the entire collision process. It comprises normal contact force, tangential frictional force during contact, and lubrication force. The contact model employed here, accounting for the laps of time when particle surfaces actually touch, is an extension of the approach of Tschisgale et al. [53] to particulate flow and was published in a companion paper [24]. For the normal contact force, the Poisson hypothesis is used stating that the normal relative speed at the contact point of a colliding pair of particles after the collision, $\mathbf{u}_{r,n}^n$, equals the restitution coefficient $e_{d,n}$ times the normal relative speed before collision, $\mathbf{u}_{r,n}^{n-1}$, i.e.

$$\mathbf{u}_{r,n}^n = -e_{d,n}\,\mathbf{u}_{r,n}^{n-1}\,. \tag{6}$$

Analogously, the tangential frictional force is calculated using a tangential restitution coefficient $e_{d,t}$. Later, the tangential frictional force is adjusted in order to allow the sliding of the particles using the well-known Coulomb friction law, which states that the particles stick if $f_t \leq \mu_s f_n$ and slide otherwise. Here, f_n and f_t are the magnitudes of the contact forces in normal direction, i.e. in direction of $\mathbf{n}$, and in tangential direction, with $\mathbf{t}$ the appropriate tangential unit vector, respectively. The factor μ_s represents the static coefficient of friction which in the present work is assumed to equal the kinetic coefficient of friction, μ_k. In the case of sticking, the force calculated earlier

is a good approximation, whereas in the case of sliding, the tangential frictional force is modified to

$$f_t = \mu_k f_n\,. \tag{7}$$

Prior and after particle surfaces truly touch, lubrication forces act between the particles during approach and rebound as soon as the surfaces come close. These forces need to be captured by a so-called lubrication model. A new model of this kind was recently developed by the present authors. In contrast to other models, such as the ones of Cox and Brenner [10], Jeffrey [25], Kempe and Fröhlich [28], Izard et al. [22], Costa et al. [9], in this model the lubrication forces are taken to be constant over distance conserving the integral of the force over the unresolved distance, as illustrated by Fig. 1. As a result, the force is constant in time during the approach. This model offers numerical robustness and physical realism, as demonstrated in [24]. A detailed description and a thorough validation can be found in that as well.

3 Computational setup

3.1 Channel geometry and resolution

In the present work, a turbulent open channel flow with periodic boundary conditions in streamwise and spanwise direction is considered with a free-slip condition at the top, also called rigid lid, and a no-slip condition at the bottom wall and at the particle surfaces. The size of the computational domain is $L_x \times L_y \times L_z$, with $N_x \times N_y \times N_z$ the corresponding number of grid points. A set of $N_{p,mob}$ particles with density ρ_p and relative submerged density $\rho' = (\rho_p -$
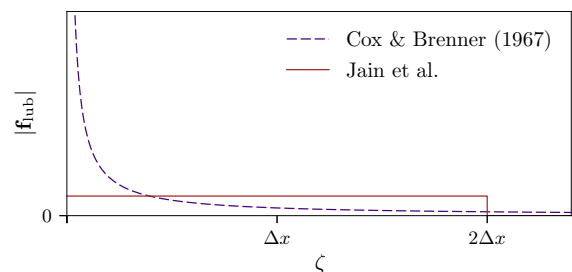
Fig. 1 Lubrication model as a function of the distance ζ between the colliding surfaces, Δx is the stepsize of the Eulerian grid. Dotted line: relation of Cox and Brenner [10]. Solid line: relation proposed by Jain et al. [24]

$\rho_f)/\rho_f$ travel over a rough bottom wall made of immobile particles of the same diameter D_{eq}. This rough wall is constituted of a single layer of $N_{p,sed}$ fixed spheres in a hexagonal packing. To introduce non-uniform roughness, the wall-normal position of the fixed particles was varied by a random displacement $\Delta_{y,p}$, as described in [23]. The chosen interval for the displacement is $-0.5D_{eq} < \Delta_{y,p} < 0.5D_{eq}$. For all positive displacements, another particle was introduced underneath the displaced one to fill the hole as depicted in Fig. 2. The importance of such a bed was thoroughly discussed in the cited reference.

In the simulations, a spatially constant volume force $\mathbf{f}_v(t)$ is applied to drive the flow, and is adjusted instantaneously in time to maintain the desired flow rate, so that a constant bulk Reynolds number Re_b is imposed. The friction velocity u_τ is calculated by extrapolating the linear profile of the total shear stress of a simulation without mobile particles down to the interface between the mean height of the fixed particles and the flow, i.e. at a distance $H_{sed} = 1\,D_{eq}$ from the bottom wall (Fig. 2), which is taken as the origin of the wall-normal coordinate y. The same methodology was used in [30] and [54]. The physical parameters of the present simulations are summarized in Table 1. The bulk Reynolds number $Re_b = U_b H/\nu_f$ was imposed to be 3010 with the bulk velocity defined as $U_b = \frac{1}{H}\int_0^H \langle u \rangle (y)\,dy$ and the submergence height $H = L_y - H_{sed}$. Angular brackets indicate averaging as specified below. The Reynolds number based on the above friction velocity is $Re_\tau = u_\tau H/\nu_f = 270$ yielding a diameter in wall units of $D_{eq}^+ = u_\tau D_{eq}/\nu_f = 30$. Another important nondimensional parameter in
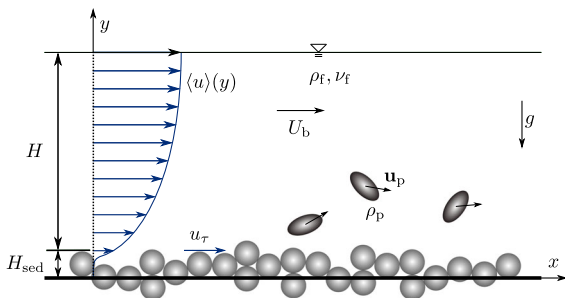

Fig. 2 Schematics of the flow above the irregular sediment bed in an open channel with transport of few mobile particles investigated in the present study and physical parameters describing the problem

particulate flow is the Galileo number, which is defined as the ratio of gravity forces to viscous forces, i.e. $Ga = \sqrt{\rho' g D_{eq}^3}/\nu \approx 138$. To provide the same roughness from the fixed bed in all simulations the same arrangement of spherical particles was used throughout. The particle volume fraction in all simulations is $\approx 7.5\%$. The domain was discretized with $1024 \times 197 \times 512$ grid cells. As a result, the particle discretization is $D_{eq}/\Delta x = 19.7$. The resolution in terms of wall units is $\Delta x^+ = u_\tau \Delta x/\nu_f = 1.54$. The time step was adaptively adjusted to yield a *CFL* number of 0.6.

3.2 Mobile particles

The mobility of a particle at the top of a sediment bed is commonly assessed by the Shields number

$$Sh = u_\tau^2/(\rho' g D_{eq}). \tag{8}$$

Here, $\rho' = 1.5$, i.e. $\rho_p/\rho_f = 2.5$ was used as this is a good approximation for quartz sand in water. With $g = 0.115\,U_b^2/D_{eq}$ it yields $Sh = 0.047$ which is above the critical value of incipient motion, $Sh_{crit} = 0.034$, taken from the graph presented in the original paper of Shields [49] and, hence, suggests that the particles are mobile.

A total of four different simulations were conducted each differing only in the shape of the mobile particles (Table 2). In particular the volumetrically equivalent diameter D_{eq} and the relative density ρ' were taken to be identical. The shapes considered are ellipsoids with $a \geq b \geq c$ designating the three half axes, so that $D_{eq} = 2\sqrt[3]{abc}$. The axes ratios $b\,/\,a$ and $c\,/\,b$ are the parameters used by Zingg [56] to classify the shape of a particle into four categories (disk, equant, blade, rod). For a quantitative comparison of particles, this classification is one of the most valuable schemes [2] and still widely used today. After measuring approximately 300 particles, the ellipsoid with $b/a = 0.67$ and $c/b = 0.67$ was found to be the average shape in the parameter space spanned by $b\,/\,a$ and $c\,/\,b$. The ratio 0.67 was then used by Zingg to divide both axes, $b\,/\,a$ and $c\,/\,b$, for a quantitative definition of the four categories of shapes mentioned [56]. This shape is employed here for reference and is addressed as "*Zingg-ellipsoid*" in the following.

Table 1 Domain size, spatial resolution, and other common parameters in all the simulations

L_x/D_{eq}	L_y/D_{eq}	L_z/D_{eq}	N_x	N_y	N_z	$N_{p,sed}$	$N_{p,mob}$	$D_{eq}/\Delta x$	D_{eq}^+	Δx^+
52	10	26	1024	197	512	2331	500	19.6	30.3	1.54

Table 2 Geometrical parameters of the mobile particles in the cases simulated with a, b, c the half-axes of the ellipsoid, ψ its sphericity and N_L the number of Lagrange markers on the particle surface

Case	a/D_{eq}	b/D_{eq}	c/D_{eq}	$a : b : c$	ψ	N_L
Zingg-ellipsoid	0.75	0.5	0.33	1:0.67:0.44	0.66	10218
Prolate	0.78	0.4	0.4	1:0.51:0.51	0.66	10914
Oblate	0.75	0.75	0.22	1:1:0.29	0.66	11572
Sphere	0.5	0.5	0.5	1:1:1	1	9039

The sphere as well as prolate and oblate particles are special cases of an ellipsoid with $a = b = c$, $b = c$, and $a = b$, respectively. These three shapes are listed in Table 2 with the parameters employed here. The values of a, b, and c of all the non-spherical particles were calculated such that the volume is the same as that of the sphere with diameter D_{eq}. Furthermore, the sphericity of these particles is the same, $\psi = 0.66$, according to the definition of Krumbein [33]

$$\psi = \sqrt[3]{\frac{\text{Volume of an ellipsoid}}{\text{Volume of the envoloping sphere}}} = \sqrt[3]{\frac{bc}{a^2}} \ . \tag{9}$$

The snapshots in Fig. 4 below provide a visual impression of the different shapes considered. The number of Lagrange points used to represent different types of particles are assembled in Table 2. Beyond the relative density the mechanical properties of the particles are characterized by the restitution coefficient e of the material. Here, it is taken to be $e = 0.95$ which is representative of glass [27], i.e. close to that of quartz sand. The coefficient of static friction was set to $\mu_s = 0.15$ [21].

3.3 Bedload regime

With the selected values of the physical parameters, the particles travel in bedload regime, i.e. they remain very close to the bottom wall being mobilized, dislocated, occasionally deposited, and remobilized, according to the particular local and instantaneous situation. The regime addressed in this paper is the one of small particle loading [13]. A number of $N_{p,mob} =$ 500 mono-disperse and single-shaped mobile particles according to Table 2 were used in all four simulations, along with $N_{p,sed} = 2331$ fixed spherical particles constituting the bottom wall.

For small particle loading, the situation differs from the one of a thick sediment layer as described by Dietrich et al. [13]. Detailed simulations in this regime were conducted, for example, by Vowinckel et al. [54] for a Shields number of $Sh = 0.40$ and a bulk Reynolds number of $Re_b = 2941$. In this reference, monodisperse spheres were considered and only the particle loading was changed, with all other physical and numerical parameters identical. Indeed, for different particle loading, markedly different particle structures were observed ranging from pronounced ridges in streamwise direction in case of very few particles to pronounced spanwise clusters when more particles were transported. On this background the purpose of the simulations presented here is to provide a quantitative assessment of the impact of the particle shape on the motion of particles in the regime of small particle loading.

4 Results

4.1 Initialization and averaging procedures

Initially, the $N_{p,mob}$ mobile particles were placed randomly in the entire computational domain. Over a short laps of time the particles settled down while moving forward with the fluid and then continued moving in bed-load mode.
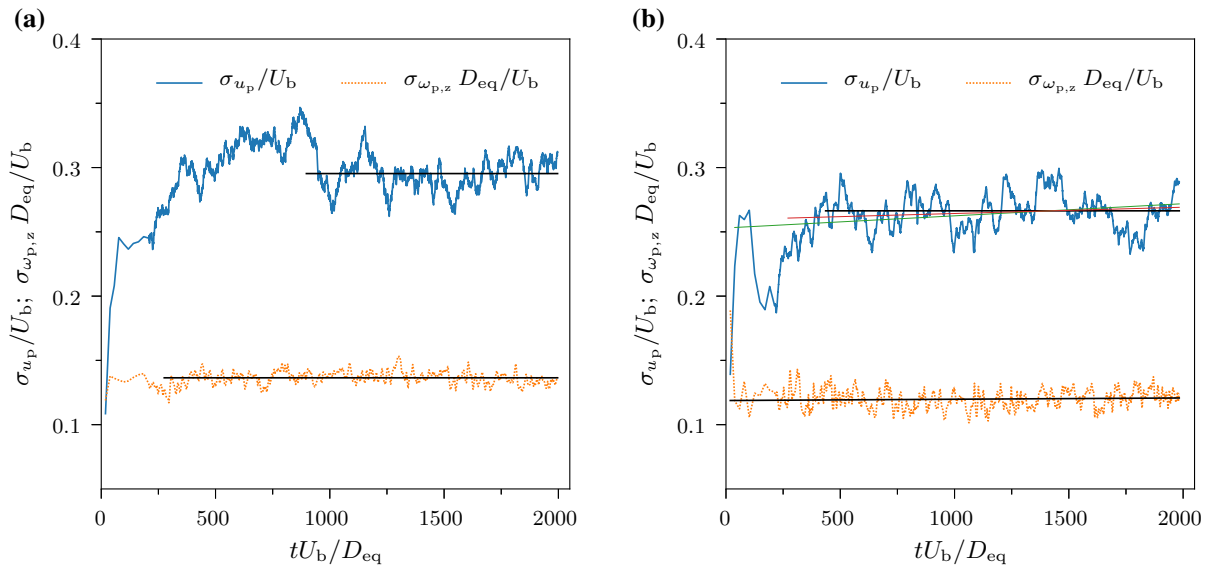
Fig. 3 Standard deviation of the streamwise particle velocity and the spanwise angular velocity as defined in (11). **a** Case *Sphere*, and **b** Case *Zingg-ellipsoid*. The black solid line is the regression line of the data starting from a time when the Pearson correlation coefficient $r \approx 0$. In (**b**) two regression lines are drawn with an earlier start and $r \neq 0$ for illustration

Before starting any averaging, it is important to assure that there is no influence of the initial conditions on the statistical quantities. In general, the time scale over which particle structures develop, if any, is substantially larger than the time taken in the development of fluid structures. Therefore, the temporal variation of the second order statistics of the streamwise particle velocity u_p and spanwise angular velocity of the particles, $\omega_{\mathrm{p},z}$ was observed. Averaging was started when the standard deviation in u_p and $\omega_{\mathrm{p},z}$ calculated according to Eq. (11) was no more correlated with time. This condition ensures that erosion and deposition are in equilibrium.

Technically, this was implemented starting from the average particle velocity at a given time defined as

$$\bar{u}_\mathrm{p}(t) = \frac{1}{N_\mathrm{p,mob}} \sum_{i=1}^{N_\mathrm{p,mob}} u_{\mathrm{p},i}(t) \quad , \tag{10}$$

where i is the index of an individual particle. The resulting standard deviation in u_p then is

$$\sigma_{u_\mathrm{p}}(t) = \sqrt{\frac{1}{N_\mathrm{p,mob}} \sum_{i=1}^{N_\mathrm{p,mob}} \left(u_{\mathrm{p},i}(t) - \bar{u}_\mathrm{p}(t)\right)^2} \quad . \tag{11}$$

The standard deviation of the spanwise angular velocity, $\sigma_{\omega_{\mathrm{p},z}}$, was calculated analogously. For

illustration, σ_{u_p} and $\sigma_{\omega_{\mathrm{p},z}}$ are plotted against time in Fig. 3 for the cases *Sphere* and *Zingg-ellipsoid*. Subsequently, a linear regression analysis using the least square method was performed and the Pearson correlation coefficient r determined. First, the entire dataset was used. Then, if $r \neq 0$, the start of the data in the analysis was changed to a later instant. This was repeated until $-10^{-4} \leq r \leq 10^{-4}$ implying that the two variables, i.e. σ_{u_p} and t, are not correlated to each other. Three such iterations are shown in Fig. 3b for illustration. The starting point obtained in this way was retained for all subsequent averages in a particular simulation. The starting time for averaging t_in and the averaging period T_av of all simulations are tabulated in Table 3.

With t_in being fixed, averages of fluid quantities were computed over the streamwise direction, the spanwise direction, and in time on the Eulerian grid, i.e. on the staggered grid of the flow solver. For technical reasons the data were then linearly interpolated to the grid constituted by the cell centers, so that all fluid statistics were available on the same grid. Points lying inside the particles were excluded from this average. This was implemented defining a porosity field $\phi(\mathbf{x}, t)$ such that $\phi = 0$ in a cell if the cell centre lies within a particle, and $\phi = 1$ else. Therefore, an averaged fluid-related quantity θ is

Table 3 Initial time t_{in} before the averaging procedure was started and the time interval T_{av} during which statistical averaging was conducted for the different cases

	Zingg-ellipsoid	Prolate	Oblate	Sphere
$t_{in} U_b/D_{eq}$	436.08	735.8	862.11	897.51
$T_{av} U_b/D_{eq}$	1546.97	917.40	1130.54	1099.02

$$\langle \theta \rangle(y) = \frac{1}{T_f} \frac{1}{V_f} \int_{t_{in}}^{t_{in}+T_{av}} \int_{V_0} \phi(\mathbf{x},t)\,\theta(\mathbf{x},t)\,\mathrm{d}V\,\mathrm{d}t, \qquad (12)$$

where $T_f V_f = \int_{t_{in}}^{t_{in}+T_{av}} \int_{V_0} \phi(\mathbf{x},t)\,\mathrm{d}V\,\mathrm{d}t$. Here, V_f is the part of the volume V_0 occupied by fluid and T_f is the total time when the volume V_0 was occupied by fluid even briefly. Such an averaging procedure is known as intrinsic averaging [37]. According to Jain et al. [23], an averaging volume $V_0 = L_x \times 4\Delta y \times L_z$ was used. The particle-related fields were calculated using

$$\theta_p(\mathbf{x},t) = \sum_{i=1}^{N_{p,mob}} (1 - \phi^i(\mathbf{x},t))\,\theta_p^i(t). \qquad (13)$$

with ϕ^i the mask $\phi(\mathbf{x},t)$ generated by the ith particle, and θ_p^i any physical quantity of the ith particle. Then, the intrinsic averaging as in Eq. (12) was applied to determine the average particle-related quantities.

4.2 Qualitative observations

Visualizations show that the movement of all four types of particles along the bed is strongly affected by their shape. For spherical particles the following is observed. While saltating they are lifted up, then fall steadily and mostly rebound after an impact with the bed. This is followed by a rolling motion before coming to rest until a new lift off takes place. In contrast, the oblate particles have a flatter and lengthier trajectory followed by a collision with stronger damping and a sliding motion.

Prolates and Zingg-ellipsoids, once lifted, show a steady fall with slightly prolonged trajectory. In these cases the rebound is minimal and both rolling and sliding behavior is noticed, depending upon the particle orientation. Four instantaneous pictures obtained from the four simulations are shown in Fig. 4. They indicate that the spheres jump quite high,

whereas the other three types of particles stay closer to the bed. The non-spherical particles seem to orient with their maximum projection area parallel to the flow. Their orientation on the bed is highly influenced by the fixed particles as they pivot around them. Additionally, larger fluctuations in the streamwise fluid velocity can be noticed in the cases with non-spherical particles, as visualized by the iso-surfaces in Fig. 4.

4.3 Mean flow and Reynolds stresses

Figure 5 displays the mean velocity profile for all cases investigated. These data show that the particle shape has almost no effect on the mean velocity in this flow. This can be due to the small volume fraction of mobile particles with most of the channel roughness introduced by the fixed bed which is the same in all the simulations. Recently, Eshghinejadfard et al. [18] also found that in simulations with spherical and oblate particles at low concentration the mean profiles of the streamwise fluid velocity exhibited only subtle differences. Only when the concentration of oblate spheroids was increased in that reference, there were recognizable changes close to the channel center.

Figure 6 shows the four non-vanishing components of the Reynolds stress tensor normalized with the bulk velocity. In Fig. 6a it is observed that the streamwise Reynolds stress $\langle u'u' \rangle$ in the case *Sphere* is approximately 25% smaller than for the other three cases in the region of particle presence. While the profiles are similar in the upper region of the channel. Also, there is not much difference between the profiles obtained with the different non-spherical particles compared to the results for spheres. In Fig. 6b, the wall-normal fluctuations $\langle v'v' \rangle$ are plotted. They are maximum in the case *Oblate* and minimum in the case *Sphere*. Not only are the peak values different, but also the location of the peaks is shifted towards the channel center, from sphere to oblate. The profiles of the case *Zingg-ellipsoid* and *Prolate* lie between those of the other cases. The Reynolds shear stress $\langle u'v' \rangle$ shows a similar behavior as $\langle v'v' \rangle$. The spanwise component $\langle w'w' \rangle$ is very much the same for all non-spherical particles, exhibiting a marked difference from the result obtained with spheres.
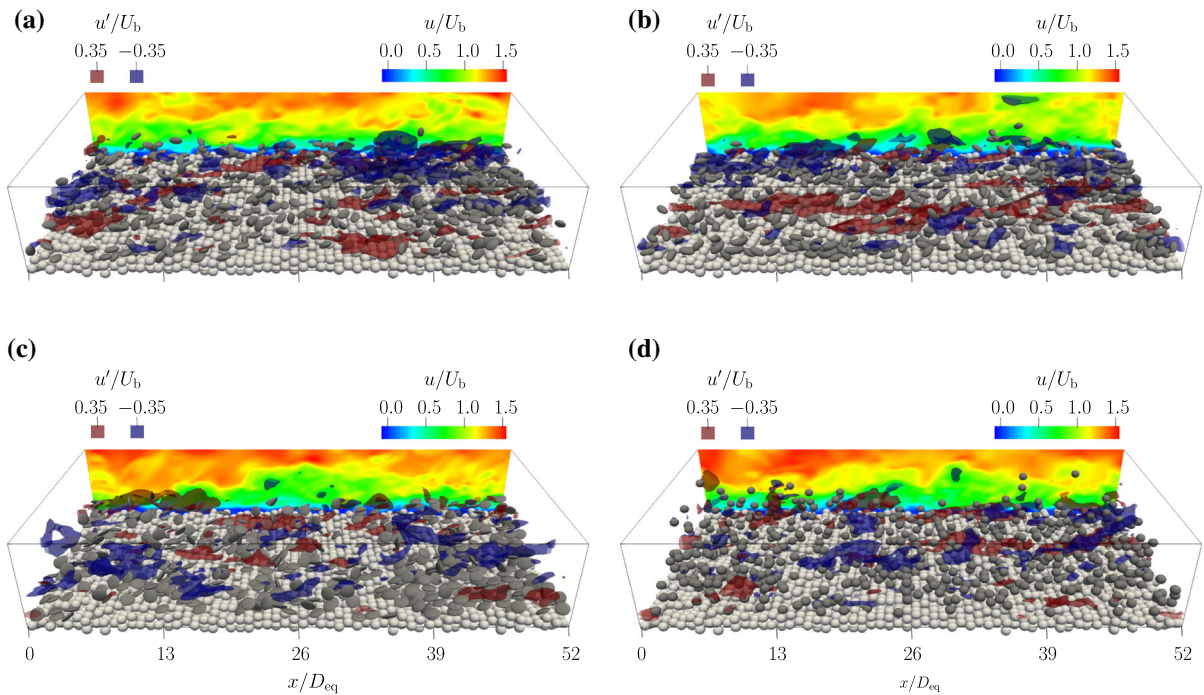
Fig. 4 Instantaneous snapshots of the four simulations presented using the same plot style at an arbitrary instant in time with flow from left to right. **a** Zingg-ellipsoids, **b** prolates, **c** oblates, **d** spheres. The contour plots show the streamwise velocity field at this instant while iso-surfaces represent the velocity fluctuations. Fixed and mobile particles are colored light and dark gray, respectively
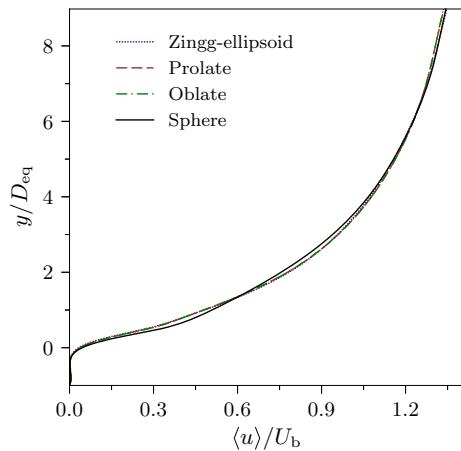

Fig. 5 Effect of particle shape on averaged streamwise component of the fluid velocity normalized with the bulk velocity

4.4 Mean particle position and mean velocity

Figure 7 shows the wall normal profile of the volume fraction occupied by the mobile particles. It is seen that the spherical particles travel up to $y \approx 5\,D_{eq}$, whereas the highest particle position obtained for the other three shapes is $y \approx 4\,D_{eq}$. The volume occupied by the spherical particles at $y = 2D_{eq}$ is almost twice the volume occupied by particles of the other shapes. Instead, non-spherical particles are more frequently observed in the near-wall region, $0 < y/D_{eq} < 1$. The differences in the peaks of $\langle \gamma \rangle$ for oblate, prolate, and Zingg-ellipsoid particles are due to their pivoting position around protruding particles constituting the fixed bed. Animations show that some of the Zingg-ellipsoids can occasionally enter the troughs of the irregular sediment bed, whereas oblate particles mainly rest on top of them. The probability of finding the non-spherical particles in this region is almost the same.

The averaged streamwise particle velocity is plotted against the wall normal coordinate in Fig. 8a. Since the number of particles above $y = 3\,D_{eq}$ is too small to obtain converged statistics the curves are only shown in the region $-H_{sed} < y < 3D_{eq}$. The graph demonstrates that the spherical particles move faster near the bed than the other three types of particles,
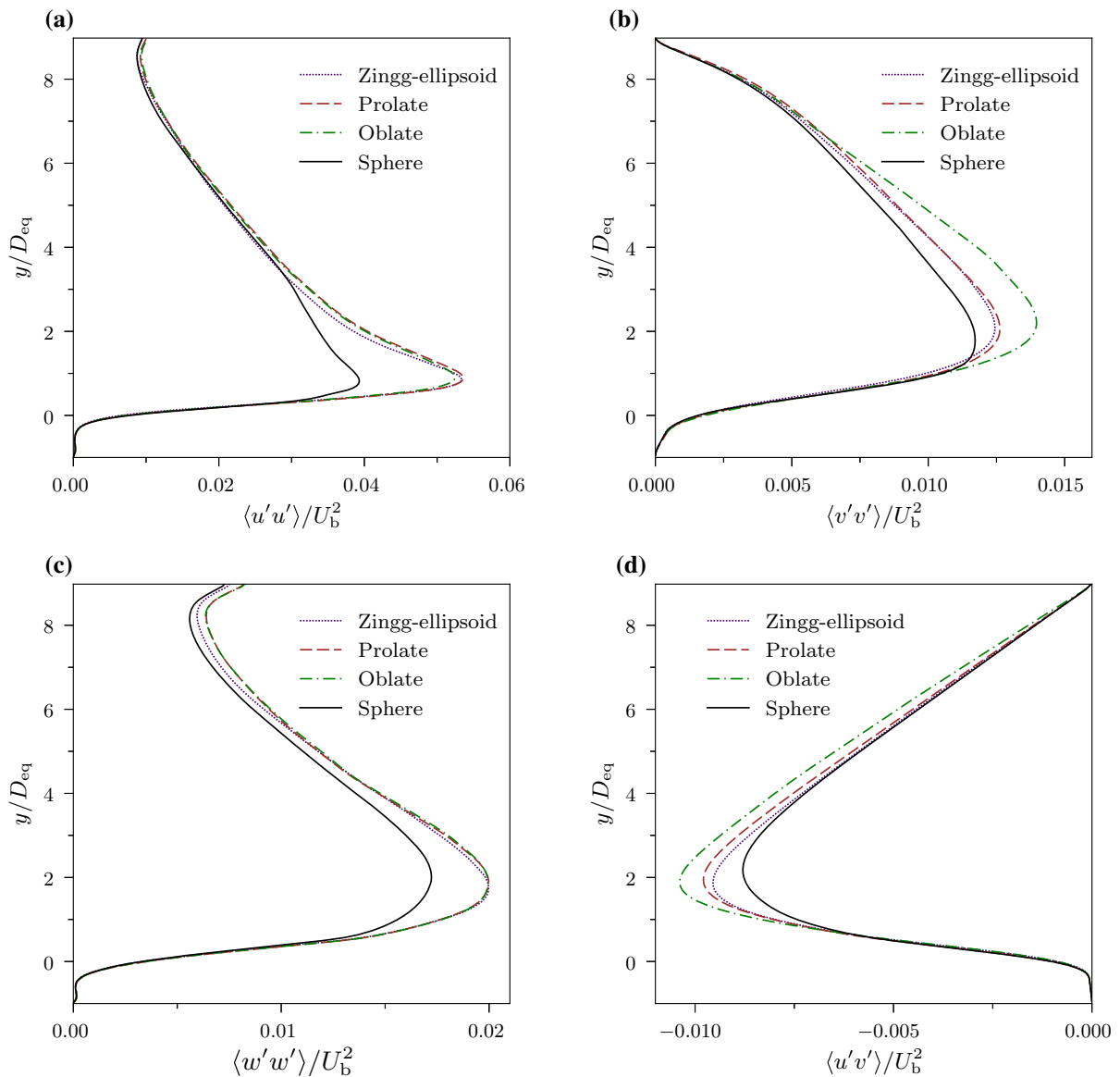
(a)

(b)

(c)

(d)

Fig. 6 Wall normal profiles of Reynolds stresses normalized with the bulk velocity. **a** Streamwise component $\langle u'u'\rangle/U_\mathrm{b}^2$, **b** wall-normal component $\langle v'v'\rangle/U_\mathrm{b}^2$, **c** spanwise component $\langle w'w'\rangle/U_\mathrm{b}^2$, and **d** shear stress $\langle u'v'\rangle/U_\mathrm{b}^2$

whereas in the clear water the spheres, prolates, and Zingg-ellipsoids have a similar translational velocity and oblate spheroids move slowest among all the particles. Above $y \approx 1\,D_\mathrm{eq}$, oblate spheroids have the largest relative velocity with respect to the fluid, since they move slowest, with a marked difference. The relative mean particle velocity was determined according to $\langle u_\mathrm{r}\rangle = \langle u_\mathrm{p}\rangle - \langle u\rangle$, as discussed in detail by Santarelli and Fröhlich [46], and is shown in Fig. 8b. The Zingg-ellipsoids have the largest relative

velocity with respect to the fluid in the near wall region $y \approx 0.5\,D_\mathrm{eq}$ and spheres have the smallest. In contrast, spheres move fastest, so that their relative velocity is smaller. The Reynolds number $Re_\mathrm{p} = |\langle u_\mathrm{r}\rangle|D_\mathrm{eq}/\nu$, is $Re_\mathrm{p} \approx 62$ at the elevation $y = 0.57\,D_\mathrm{eq}$ in the case *Zingg-ellipsoid* and is $Re_\mathrm{p} \approx 49$ in the case *Sphere* at the same elevation. The negative relative particle velocity near the wall at $y = 0.5D_\mathrm{eq}$ is in contrast with the results for neutrally buoyant particles reported in
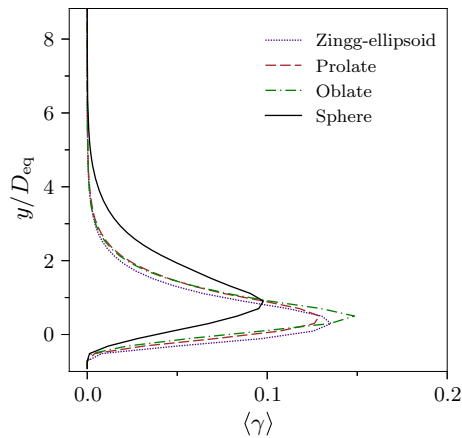
Fig. 7 Effect of particle shape on the average particle position. Wall-normal profiles of the PDF of the wall-normal coordinate of the particle center

[3] where a larger mean particle velocity, compared to the mean fluid velocity, was observed.

The wall-normal profile of the spanwise angular velocity for the cases simulated is shown in Fig. 9. The data reveal that the preferred mode of transport changes substantially between the different particle shapes. Spherical particles roll, whereas oblate spheroids predominantly slip. These results are supported by the experimental observations of Krumbein [34] and Rice [43], for example. The small magnitude of the angular velocity near the bed in the case *Oblate*

is caused by two different effects, which is backed by corresponding animations analyzed by the authors. One is that a hit with the irregular sediment bed often causes an oblate particle with high momentum to rotate. Second, an oblate spheroid may roll if it is pivoting such that its maximum projected area is roughly parallel to the *xy*-plane. A prolate spheroid, in contrast, is prone to rotate if its longest axis is oriented in spanwise direction. A higher value of the angular velocity in the case *Prolate*, furthermore, suggest that more prolate spheroids than oblates are in rolling motion. The Zingg-ellipsoids have an angular velocity in between the other cases. These observations can be traced back to the preferential orientation of the particles, so that this is now studied in detail.

4.5 Second moments of the particle velocities

The second central moments of the particle velocities along with the covariance between u_p and v_p are shown in Fig. 10. For the spherical particles the variance in the streamwise particle velocity, $\langle u'_p u'_p \rangle / U_b^2$, is the largest among the four cases inside the irregular sediment bed, i.e. for $y < 0.5\,D_{eq}$ and it is the smallest for $y > 1\,D_{eq}$ (Fig. 10a). Among all non-spherical cases, the oblate spheroids have the smallest fluctuations in the near wall region $0.5\,D_{eq} < y < 2\,D_{eq}$. The mean squared fluctuations in the wall-normal particle
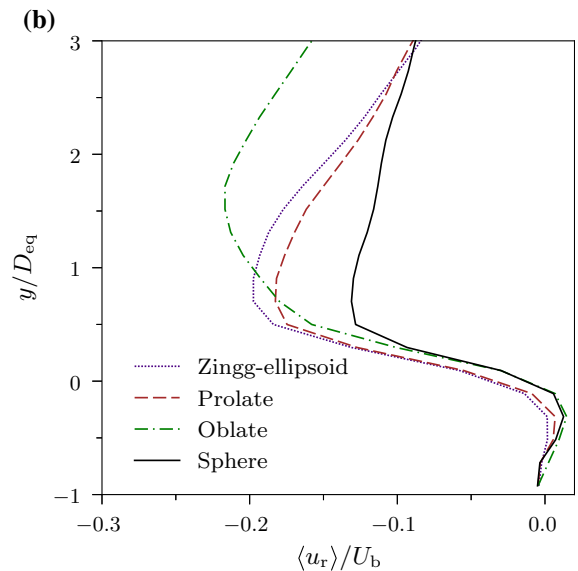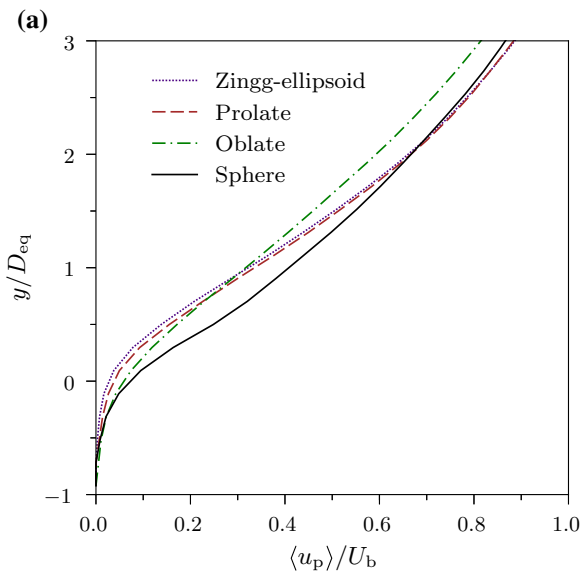

Fig. 8 Mean particle velocity. **a** Averaged streamwise particle velocity, **b** averaged streamwise particle velocity relative to the mean streamwise fluid velocity
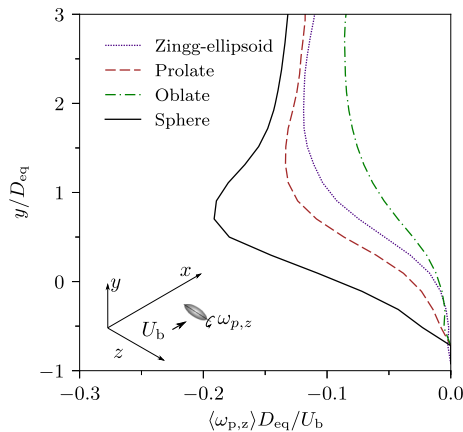
Fig. 9 Mean angular velocity in the spanwise direction plotted against distance from the wall

velocity, $\langle v'_\mathrm{p} v'_\mathrm{p} \rangle / U_\mathrm{b}^2$, are largest in the case *Sphere* throughout the channel height as shown in Fig. 10b. The difference between the spherical and the non-spherical cases is maximum in the near wall region, e.g. at $y \approx 0.6\,D_\mathrm{eq}$. Here, the variance $\langle v'_\mathrm{p} v'_\mathrm{p} \rangle / U_\mathrm{b}^2$ with spherical particles is approximately 2.5 times the value observed in the non-spherical cases. The second moment of the spanwise particle velocity, $\langle w'_\mathrm{p} w'_\mathrm{p} \rangle / U_\mathrm{b}^2$, is shown in Fig. 10c. This quantity is also an indication to the dispersive nature of a particle trajectory [36], termed "diffusion" in that reference. For $y < 1.1\,D_\mathrm{eq}$ the fluctuations in w_p are largest in the case *Sphere*, whereas above $y \approx 1.1\,D_\mathrm{eq}$ the trajectories of oblate spheroids are more dispersive. Analogous to Fig. 10b, the covariance between u_p and v_p is largest in the case of spherical particles, as shown in Fig. 10d. The profiles for the case *Zingg-ellipsoid* and *Prolate* are similar in all sub-figures shown in Fig. 10.

4.6 Statistics of particle orientation

The results shown in the previous subsection give rise to further questions: How often do particles orient themselves such that they can roll? Does the shearing flow have a sizable impact in case of such an orientation or does this happen randomly after a collision with the bed?, etc. To explore the particle orientation in detail, two sets of unit vectors are defined as shown in Fig. 11a, $\mathbf{e_x}$ pointing in the streamwise direction and $\mathbf{e_y}$ in the wall-normal direction. The unit vectors aligned with the longest

and the shortest axis of a particle are $\mathbf{d}_1$ and $\mathbf{d}_3$, respectively. Then, the absolute value of the scalar products $|\mathbf{d}_1 \cdot \mathbf{e_x}|$ and $|\mathbf{d}_3 \cdot \mathbf{e_y}|$ can be used to assess the particle orientation. Observe that any alignment of a particle on the surface of the cone shown in Fig. 11b gives the same magnitude of the scalar product $|\mathbf{d}_1 \cdot \mathbf{e_x}|$.

First, the PDF of $|\mathbf{d}_1 \cdot \mathbf{e_x}|$ is plotted in Fig. 12a. It was obtained using 100 bins for the values $|\mathbf{d}_1 \cdot \mathbf{e_x}|$. In the case *Sphere*, the PDF is unity for all angles, as it should be, demonstrating that no numerical bias is present. The probability of prolate spheroids and Zingg-ellipsoids to align their longest axis in the streamwise direction is higher than for aligning it perpendicular to the flow. Because of its shape, a prolate with its smaller axis oriented in the *xy*-plane is easier to roll by the shearing flow than a prolate with its longest axis in the streamwise direction. Since the probability of an alignment in the latter position is higher than for the other orientations the prolates have less spanwise angular velocity $\omega_{\mathrm{p},z}$. Figure 12b with the PDF of $|\mathbf{d}_3 \cdot \mathbf{e_y}|$ can be interpreted in a similar way. The oblate spheroids orient such that their symmetry axis, i.e. their shorter axis, points in the wall-normal direction. An oblate with such an orientation is difficult to roll.

Comparing Fig. 12a, and Fig. 12b shows that the oblate spheroids having an orientation which hinders the rolling motion in the streamwise direction is more probable than a prolate in an analogous orientation. The probability of $|\mathbf{d}_3 \cdot \mathbf{e_y}| > \sqrt{2}/2$ in the case *Oblate* is $\approx 72\%$, whereas $|\mathbf{d}_1 \cdot \mathbf{e_x}| > \sqrt{2}/2$ in the case *Prolate* is $\approx 52\%$. In other words, the probability of the oblate particles having an orientation that eases the rolling motion is only $\approx 28\%$ in comparison to the value of $\approx 48\%$ in the case of prolate spheroids. Therefore, the angular velocities are so different, even though both particles are circular in a plane. Zingg-ellipsoids preferentially move with their longest axis directed along the streamwise direction and the shortest axis along the wall-normal direction, on average.

The curve for oblates is not plotted in Fig. 12a since with the short axis fixed the "long axis" can have an arbitrary orientation in the plane perpendicular to the short axis and, hence, carries no new information. The same holds for the "short axis" of the prolate particles so that this curve was removed from Fig. 12b. For the Zingg-ellipsoid with three different axes such an
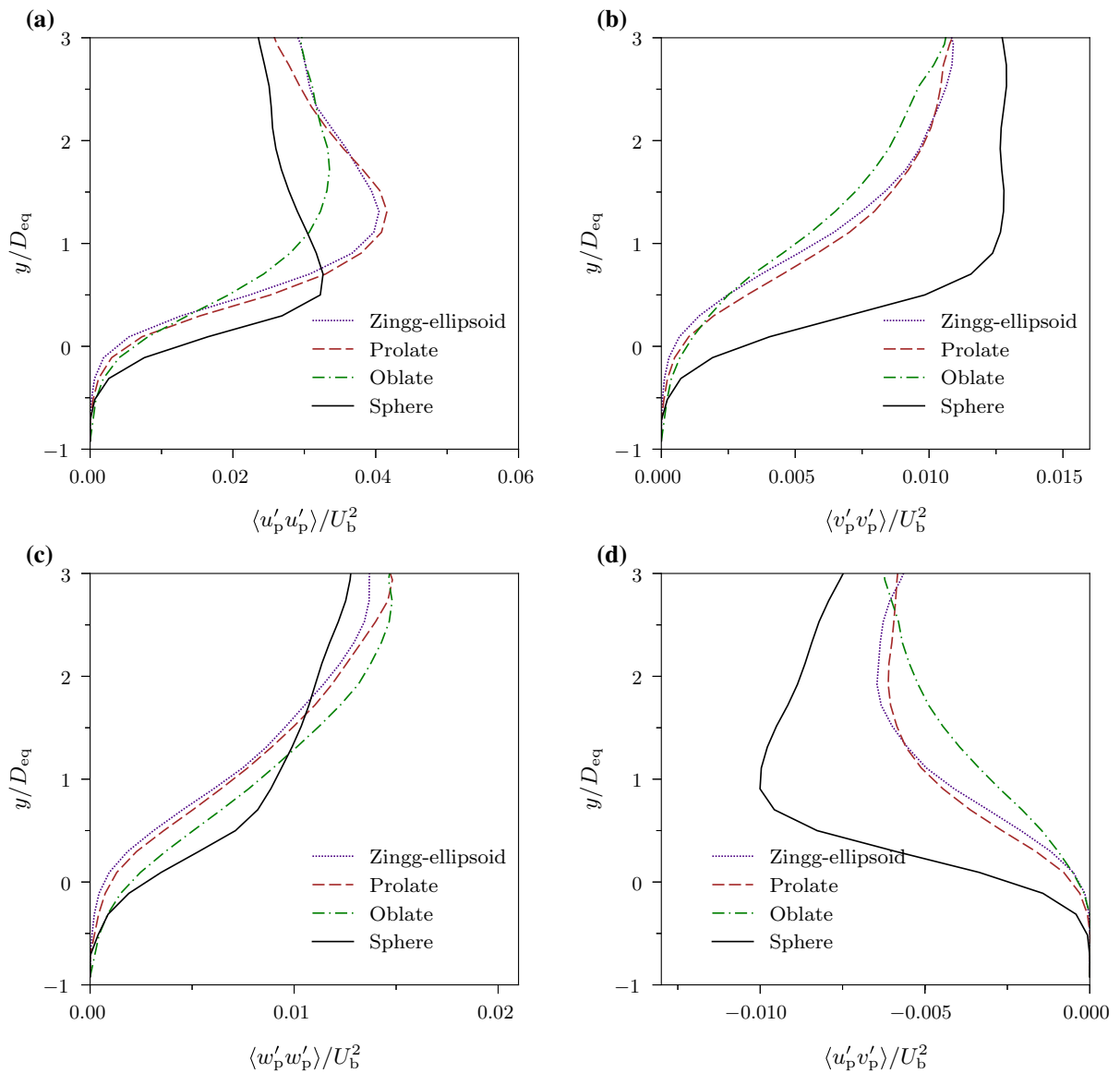
Fig. 10 Wall normal profiles of the second moments of particle velocity normalized with the bulk velocity. **a** Streamwise component $\langle u'_\mathrm{p} u'_\mathrm{p} \rangle / U_\mathrm{b}^2$, **b** wall-normal component $\langle v'_\mathrm{p} v'_\mathrm{p} \rangle / U_\mathrm{b}^2$, **c** spanwise component $\langle w'_\mathrm{p} w'_\mathrm{p} \rangle / U_\mathrm{b}^2$, and **d** covariance between u_p and v_p, $\langle u'_\mathrm{p} v'_\mathrm{p} \rangle / U_\mathrm{b}^2$

argument does not hold so that the curves are retained in both graphs.

To see the effect of the shearing fluid on the particle orientation, the wall-normal profiles of $\langle |\mathbf{d}_1 \cdot \mathbf{e_x}| \rangle$ and $\langle |\mathbf{d}_3 \cdot \mathbf{e_y}| \rangle$ are plotted in Fig. 13. To determine these quantities, the height of the channel was divided into a set of bins. If a particle center lies inside a bin, $|\mathbf{d}_1 \cdot \mathbf{e_x}|$ and $|\mathbf{d}_3 \cdot \mathbf{e_y}|$ of the particle are assigned to this bin. As suggested by Kempe et al. [30], the width of the bin was set to $D_\mathrm{eq}/10$. It is clearly seen that the particles

align themselves in their preferential orientations well above the wall with an increasing trend towards the wall. Prolates orient their long axis in streamwise direction, oblates orient their short axis normal to the mean flow. This tendency is most pronounced near the bottom and reduces in upward direction but is still seen at $y \approx 3\,D_\mathrm{eq}$. Again, the line corresponding to the case *Zingg-ellipsoid* is in between the cases *Oblate* and *Sphere*. The values for the sphere are 0.5 uniform, as they should.
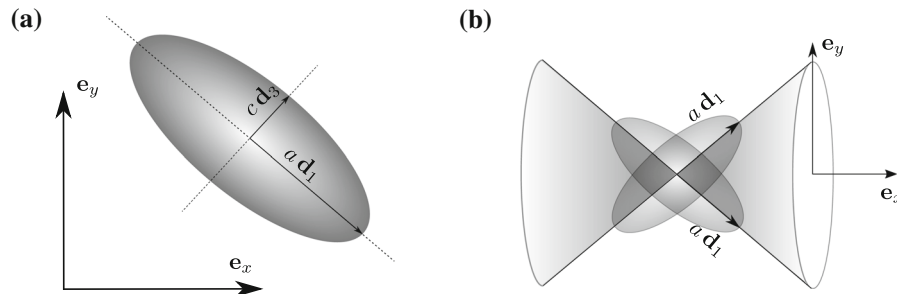
(a)

(b)

Fig. 11 Sketches illustrating the assessment of the particle orientation. **a** Unit vectors in streamwise and wall-normal direction, $\mathbf{e}_x$ and $\mathbf{e}_y$, respectively, together with the unit vectors

in direction of the longest and shortest axis of a particle, $\mathbf{d}_1$ and $\mathbf{d}_3$, respectively. **b** Possible orientations of a particle in 3D that result in the same value of $|\mathbf{d}_1 \cdot \mathbf{e_x}|$

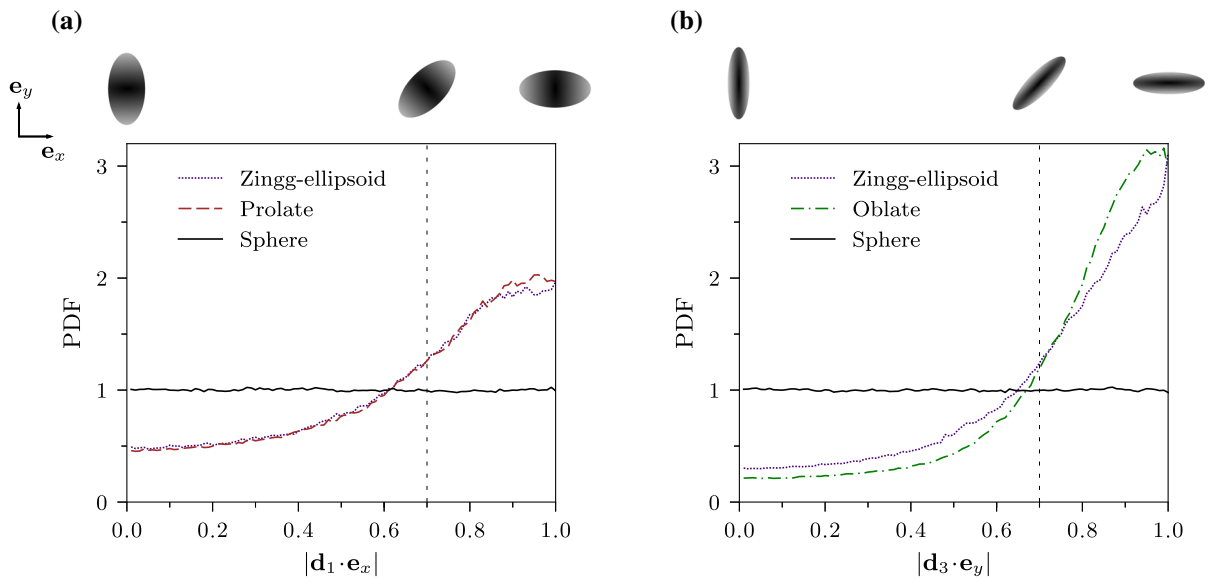**(a)**

(b)

Fig. 12 Statistics of particle orientation. **a** PDF of $|\mathbf{d}_1 \cdot \mathbf{e_x}|$. Three exemplary orientations of the prolate-shaped particle are shown on top of the graph with $|\mathbf{d}_1 \cdot \mathbf{e_x}| = \mathbf{0}$, $\sqrt{2}/2$, and 1. **b** PDF of $|\mathbf{d}_3 \cdot \mathbf{e_y}|$. Three exemplary orientations of the oblate-shaped

particle are shown with $|\mathbf{d}_3 \cdot \mathbf{e_y}| = \mathbf{0}$, $\sqrt{2}/2$, and 1. The vertical dashed line indicates the value $\sqrt{2}/2$ corresponding to an inclination by 45 degrees

Similar results were found for non-buoyant, i.e. non-sedimenting, prolate spheroids in [17] and for oblate spheroid in [18]. Based on the fact that the mean shear is more prominent than the turbulence in the near-wall region, these authors hypothesized that the preferential orientation is due to the mean shear. In their study, the averaged orientation, i.e. $\langle |\mathbf{d}_1 \cdot \mathbf{e_x}| \rangle$ in the case *Prolate* and $\langle |\mathbf{d}_3 \cdot \mathbf{e_y}| \rangle$ in the case *Oblate*, goes towards 0.5 in clear water, where the Reynolds shear stress is the biggest contributor to the total shear stress, representing a random orientation. The present simulations, however, show a different picture since the particles still have a preferential orientation even at

$y = 3\,D_{\mathrm{eq}}$. The situation here is complex due to the interaction of several mechanisms. First, the particles are heavier than the fluid, thus experiencing frequent contact with the rough wall, so that a vertical orientation of the long axis is less favoured, for example. Second, the particles collide with the bottom and rebound during their transport also changing their angular momentum. Third, the particles exhibit a pronounced relative velocity in contrast to the non-buoyant particles in [3]. This influences their orientation similar to sedimentation. Fourth, the fluid velocity exhibits a strong gradient near the bottom, so that the particle resides in a shear flow. All of these effects
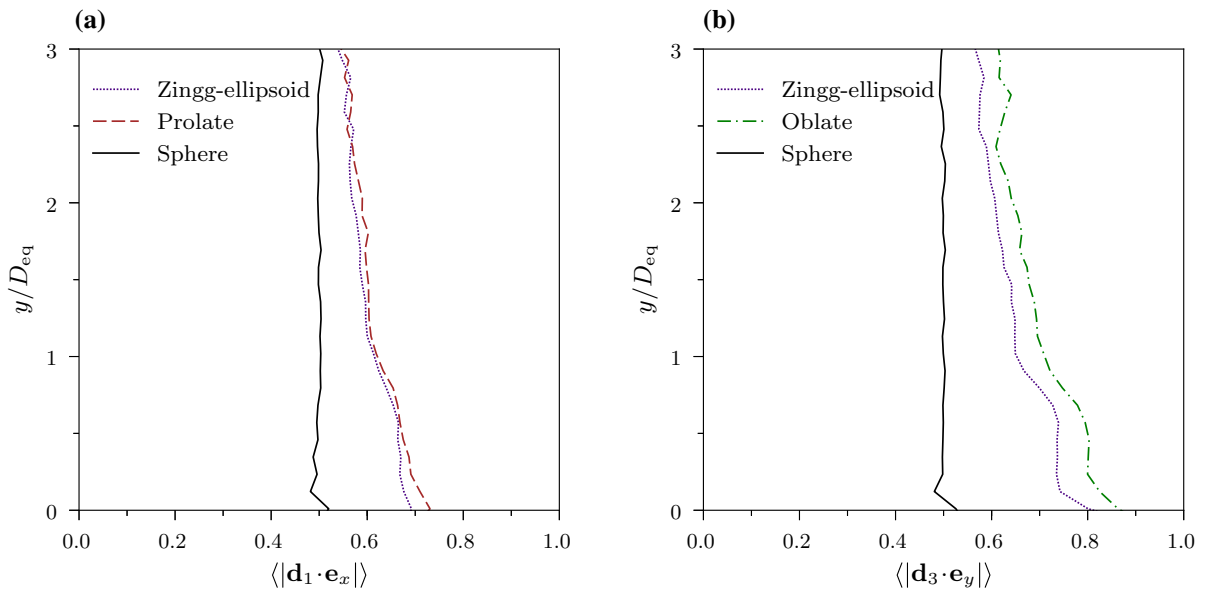
Fig. 13 Wall normal profiles of average particle orientation **a** mean scalar product between unit vector in streamwise direction, $\mathbf{e}_x$, and unit vector along the longest axis of a particle, $\mathbf{d}_1$, and **b** averaged scalar product between unit vector in wall normal direction, $\mathbf{e}_y$, and unit vector along the shortest axis of a particle, $\mathbf{d}_3$

interact. Distinguishing between them and quantifying each of them, however, seems impossible.

5 Conclusions

Direct numerical simulations of bed-load transport with geometrically resolved non-spherical particles were presented addressing the regime of low particle loading. Three simulations each with 500 mobile particles in the transitionally rough regime at $D_{eq}^+ \approx 30$ ($Re_b = 3010$) differing only in the particle shape were compared with a simulation conducted with spherical particles. In all simulations the particles have the same volume-equivalent diameter. The shape of the mobile particles appears to have a minor effect on the mean flow. However, the Reynolds stresses in the case of non-spherical particles are much higher compared to the case of spherical particles. The difference is particularly prominent in the near-wall region. The fluctuations of the streamwise and span-wise velocities in all three non-spherical cases exhibit rather small differences. The Reynolds stress components $\langle v'v' \rangle$ and $\langle u'v' \rangle$ are maximum in the case *Oblate* and minimum in the case *Sphere*. The values in the cases *Zingg-ellipsoid* and *Prolate* are in between the

two other cases. The largest differences are noticed in the particle statistics. The probability of finding a spherical particle at higher elevations is much higher than the probability of finding a non-spherical particle in this region. The spheres bounce higher with mostly a rebound after the collision with the wall, whereas non-spherical particles mostly glide near the wall and hardly rebound after a collision.

The average streamwise particle velocity in the case of spherical particles is highest near the wall, mainly due to the high angular velocity. The oblate spheroids have the least spanwise angular velocity but the second highest streamwise translational velocity near the wall. This implies that the spherical particles prefer to roll, because of their shape, whereas the oblates predominantly slide. The Zingg-ellipsoids have an angular velocity in between these two ideal cases. The oblate spheroids preferentially orient themselves with their long axis being horizontal. The prolate particles exhibit preferential orientation with their longest axis in streamwise direction. These preferential orientations are most prominent near the wall and still observed further above the sediment bed, with particle Reynolds numbers, defined with the mean relative velocity, in the range of 50.

The results obtained provide new, quantitative data on the impact of the particle shape on the mode of bed-load transport. Substantial differences were found, already for moderate variations in the shape and uniform equivalent particle diameter within each simulation. The setup is well reproducible while being close enough to a laboratory experiment, so that it can be used as a benchmark and to further exploit the parameter range concerning particle shape and composition.

References

1. Abbott JE, Francis JRD (1977) Saltation and suspension trajectories of solid grains in a water stream. Philos Trans R Soc Lond A Math Phys Eng Sci 284(1321):225–254

2. Allen JRL (1985) Principles of physical sedimentology. Springer, Dordrecht, pp 21–38

3. Ardekani MN, Brandt L (2019) Turbulence modulation in channel flow of finite-size spheroidal particles. J Fluid Mech 859:887–901

4. Ardekani MN, Costa P, Breugem WP, Picano F, Brandt L (2017a) Drag reduction in turbulent channel flow laden with finite-size oblate spheroids. J Fluid Mech 816:43–70

5. Ardekani MN, Sardina G, Brandt L, Karp-Boss L, Bearon RN, Variano EA (2017b) Sedimentation of inertia-less prolate spheroids in homogenous isotropic turbulence with application to non-motile phytoplankton. J Fluid Mech 831:655–674

6. Best J (1998) The influence of particle rotation on wake stability at particle Reynolds numbers, $Re_p < 300$—implications for turbulence modulation in two-phase flows. Int J Multiph Flow 24(5):693–720

7. Bradley WC, Fahnestock RK, Rowekamp ET (1972) Coarse sediment transport by flood flows on Knik river, Alaska. Geol Soc Am Bull 83(5):1261

8. Bravo R, Ortiz P, Perez-Aparicio J (2017) Analytical and discrete solutions for the incipient motion of ellipsoidal sediment particles. J Hydraul Res 56:1–15

9. Costa P, Boersma BJ, Westerweel J, Breugem WP (2015) Collision model for fully resolved simulations of flows laden with finite-size particles. Phys Rev E 92:053012

10. Cox RG, Brenner H (1967) The slow motion of a sphere through a viscous fluid towards a plane surface–II small gap widths, including inertial effects. Chem Eng Sci 22(12):1753–1777

11. Derksen JJ (2015) Simulations of granular bed erosion due to a mildly turbulent shear flow. J Hydraul Res 53(5):622–632

12. Dietrich WE (1982) Settling velocity of natural particles. Water Resour Res 18(6):1615–1626

13. Dietrich WE, Kirchner JW, Ikeda H, Iseya F (1989) Sediment supply and the development of the coarse surface layer in gravel-bedded rivers. Nature 340:215–217

14. Diplas P, Dancey CL, Celik AO, Valyrakis M, Greer K, Akar T (2008) The role of impulse on the initiation of particle movement under turbulent flow conditions. Science 322(5902):717–720

15. Drake TG, Shreve RL, Dietrich WE, Whiting PJ, Leopold LB (1988) Bedload transport of fine gravel observed by motion-picture photography. J Fluid Mech 192:193–217

16. El Khoury GK, Andersson HI, Pettersen B (2012) Wakes behind a prolate spheroid in crossflow. J Fluid Mech 701:98–136

17. Eshghinejadfard A, Hosseini SA, Thévenin D (2017) Fully-resolved prolate spheroids in turbulent channel flows: a lattice Boltzmann study. AIP Adv 7(9):095007

18. Eshghinejadfard A, Zhao L, Thévenin D (2018) Lattice Boltzmann simulation of resolved oblate spheroids in wall turbulence. J Fluid Mech 849:510–540

19. Fukuoka S, Fukuda T, Uchida T (2014) Effects of sizes and shapes of gravel particles on sediment transports and bed variations in a numerical movable-bed channel. Adv Water Resour 72:84–96

20. Hottovy JD, Sylvester ND (1979) Drag coefficients for irregularly shaped particles. Ind Eng Chem Process Des Dev 18(3):433–436

21. Ishibashi I, Perry C III, Agarwal TK (1994) Experimental determinations of contact friction for spherical glass particles. Soils Found 34:79–84

22. Izard E, Bonometti T, Lacaze L (2014) Modelling the dynamics of a sphere approaching and bouncing on a wall in a viscous fluid. J Fluid Mech 747:422–446

23. Jain R, Vowinckel B, Fröhlich J (2017) Spanwise particle clusters in DNS of sediment transport over a regular and an irregular bed. Flow Turbul Combust 99(3):973–990

24. Jain R, Tschisgale S, Fröhlich J (2019) A collision model for DNS with ellipsoidal particles in viscous fluid. Int J Multiph Flow 120:103087

25. Jeffrey DJ (1982) Low-Reynolds-number flow between converging spheres. Mathematika 29(1):58–66

26. Johnson TA, Patel VC (1999) Flow past a sphere up to a Reynolds number of 300. J Fluid Mech 378:19–70

27. Joseph GG, Zenit R, Hunt ML, Rosenwinkel AM (2001) Particle-wall collisions in a viscous fluid. J Fluid Mech 433:329–346

28. Kempe T, Fröhlich J (2012a) Collision modelling for the interface-resolved simulation of spherical particles in viscous fluids. J Fluid Mech 709:445–489

29. Kempe T, Fröhlich J (2012b) An improved immersed boundary method with direct forcing for the simulation of particle laden flows. J Comput Phys 231(9):3663–3684

30. Kempe T, Vowinckel B, Fröhlich J (2014) On the relevance of collision modeling for interface-resolving simulations of sediment transport in open channel flow. Int J Multiph Flow 58:214–235

31. Kidanemariam AG, Uhlmann M (2017) Formation of sediment patterns in channel flow: minimal unstable systems and their temporal evolution. J Fluid Mech 818:716–743

32. Komar PD, Reimers CE (1978) Grain shape effects on settling rates. J Geol 86(2):193–209

33. Krumbein WC (1941) Measurement and geological significance of shape and roundness of sedimentary particles. J Sediment Res 11(2):64

34. Krumbein WC (1942) Settling-velocity and flume-behavior of non-spherical particles. Eos Trans Am Geophys Union 23(2):621–633

35. Lane EW, Carlson EJ (1954) Some observations on the effect of particle shape on the movement of coarse sediments. Eos Trans Am Geophys Union 35(3):453–462

36. Nikora V, Heald J, Goring D, McEwan I (2001) Diffusion of saltating particles in unidirectional water flow over a rough granular bed. J Phys A Math Gen 34(50):L743

37. Nikora V, Ballio F, Coleman S, Pokrajac D (2013) Spatially averaged flows over mobile rough beds: definitions, averaging theorems, and conservation equations. J Hydraul Eng 139(8):803–811

38. Niño Y, García M, Ayala L (1994) Gravel saltation: 1. experiments. Water Resour Res 30(6):1907–1914

39. Ouriemi M, Aussillous P, Guazzelli É (2009) Sediment dynamics. Part 2. Dune formation in pipe flow. J Fluid Mech 636:321–336

40. Persson PO, Strang G (2004) A simple mesh generator in matlab. SIAM Rev 46(2):329–345

41. Rettinger C, Godenschwager C, Eibl S, Preclik T, Schruff T, Frings R, Rüde U (2017) Fully resolved simulations of dune formation in riverbeds. In: Kunkel JM, Yokota R, Balaji P, Keyes D (eds) High performance computing, Springer International Publishing, pp 3–21

42. Ribberink JS, Al-Salem AA (1994) Sediment transport in oscillatory boundary layers in cases of rippled beds and sheet flow. J Geophys Res Oceans 99(C6):12707–12727

43. Rice MA (1991) Grain shape effects on aeolian sediment transport. Aeolian Grain Transport 1. Springer, Vienna, pp 159–166

44. Richardson J, da Jerónimo MS (1979) Velocity-voidage relations for sedimentation and fluidisation. Chem Eng Sci 34(12):1419–1422

45. Richter A, Nikrityuk PA (2012) Drag forces and heat transfer coefficients for spherical, cuboidal and ellipsoidal particles in cross flow at sub-critical reynolds numbers. Int J Heat Mass Transf 55(4):1343–1354

46. Santarelli C, Fröhlich J (2015) Direct numerical simulations of spherical bubbles in vertical turbulent channel flow. Int J Multiph Flow 75:174–193

47. Schmeeckle MW, Nelson JM, Pitlick J, Bennett JP (2001) Interparticle collision of natural sediment grains in water. Water Resour Res 37(9):2377–2391

48. Shenoy AR, Kleinstreuer C (2008) Flow over a thin circular disk at low to moderate reynolds numbers. J Fluid Mech 605:253–262

49. Shields A (1936) Anwendung der Ähnlichkeitsmechanik und der Turbulenzforschung auf die Geschiebebewegung (in German). PhD thesis, Mitteilungen der Preußischen Versuchsanstalt für Wasserbau und Schiffbau, Berlin

50. Sun R, Xiao H (2016) Sedifoam: a general-purpose, open-source CFD-DEM solver for particle-laden flow with emphasis on sediment transport. Comput Geosci 89:207–219

51. Sun R, Xiao H, Sun H (2017) Realistic representation of grain shapes in CFD-DEM simulations of sediment transport with a bonded-sphere approach. Adv Water Resour 107:421–438

52. Tschisgale S, Kempe T, Fröhlich J (2018) A general implicit direct forcing immersed boundary method for rigid particles. Comput Fluids 170:285–298

53. Tschisgale S, Thiry L, Fröhlich J (2019) A constraint-based collision model for cosserat rods. Arch Appl Mech 89(2):167–193

54. Vowinckel B, Kempe T, Fröhlich J (2014) Fluid-particle interaction in turbulent open channel flow with fully-resolved mobile beds. Adv Water Resour 72:32–44

55. Vowinckel B, Jain R, Kempe T, Fröhlich J (2016) Entrainment of single particles in a turbulent open-channel flow: a numerical study. J Hydraul Res 54(2):158–171

56. Zingg T (1935) Beitrag zur Schotteranalyse; die Schotteranalyse und ihre Anwendung auf die Glattalschotter (in German). Schweizerische Mineralogische und Petrographische Mitteilungen 15(1):39–140